Journal of Magnetic Resonance 299 (2019) 1–11

Contents lists available at ScienceDirect

Journal of Magnetic Resonance

journal homepage: www.elsevier.com/locate/jmr

Pseudo-diffusion effects in lung MRI

C.H. Ziener [a,b], T. Kampf [c,d], F.T. Kurz [a,b], H.P. Schlemmer [a], L.R. Buschle [a,b,e,*]

[a] German Cancer Research Center - DKFZ, Im Neuenheimer Feld 280, 69120 Heidelberg, Germany
[b] Heidelberg University Hospital, Im Neuenheimer Feld 400, 69120 Heidelberg, Germany
[c] University of Würzburg, Department of Experimental Physics 5, Am Hubland, 97074 Würzburg, Germany
[d] Würzburg University Hospital, Department of Neuroradiology, Josef-Schneider-Straße 11, 97080 Würzburg, Germany
[e] Heidelberg University, Faculty of Physics and Astronomy, Im Neuenheimer Feld 227, 69120 Heidelberg, Germany

ARTICLE INFO

Article history:
Received 26 July 2018
Revised 27 November 2018
Accepted 28 November 2018
Available online 29 November 2018

Keywords:
Lung MRI
Pseudo-diffusion effects
Bloch-Torrey-equation
Susceptibility effects

ABSTRACT

Magnetic resonance imaging of lung tissue is strongly influenced by susceptibility effects between spin-bearing water molecules and air-filled alveoli. The measured lineshape, however, also depends on the interplay between susceptibility effects and blood-flow around alveoli that can be approximated as pseudo-diffusion. Both effects are quantitatively described by the Bloch-Torrey-equation, which was so far only solved for dephasing on the alveolar surface. In this work, we extend this model to the whole range of physiological relevant air volume fractions. The results agree very well with *in vivo* measurements in human lung tissue.

1. Introduction

Clinical imaging of lung tissue is typically performed with computed tomography since magnetic resonance imaging has several drawbacks: first, due to the high air volume fraction, less water molecules contribute to the signal resulting in a low signal-to-noise ratio. Second, the susceptibility effects on the air-tissue boundaries cause a fast signal decay. However, MR imaging of lung tissue continuously improves due to better MR hardware and sophisticated pulse sequences with, *e.g.*, very short echo times [1].

A main advantage of magnetic resonance imaging of lung tissue is the possibility to assess microstructural tissue parameters such as the mean alveolar size. The most common MRI technique to obtain microstructural parameters uses MR imaging of inhaled hyperpolarized gases [2,3]. Information on the microstructure can then be extracted using analytical models or numerical simulations. This approach specifically allows analyzing the respiratory tract: parameters like the lung airway size and lung branching structure [4], as well as the apparent diffusion coefficient of the gas [5] and apparent diffusion kurtosis maps [6] can be obtained. However, it is challenging to embed MR imaging with hyperpolarized gases into clinical routine since the production and application of hyperpolarized gas needs technical expertise.

Another approach to assess the lung microstructure is to directly analyze the free induction decay of the water signal. While the lineshape in most other organs is narrow and Lorentzian-shaped, lung tissue features a broad and asymmetric lineshape [7]. An analysis of the lineshape can therefore reveal microscopic changes of lung tissue [8]. To obtain microstructural parameters from measured lineshapes, it is necessary to understand the signal formation in lung tissue.

Lung tissue consists of very densely packed alveoli that are surrounded by highly vascularized tissue, see Fig. 1(a) and (b). In an external magnetic field B_0, the susceptibility difference $\Delta\chi$ between the air in the spherically-shaped alveoli and the surrounding tissue causes magnetic dipole field inhomogeneities in the form of three-dimensional dipole fields [10]:

$$\omega_{\text{dipole}}(r,\theta) = \delta\omega R_A^3 \frac{3\cos^2(\theta)-1}{r^3} = \delta\omega R_A^3 \frac{2P_2(\cos(\theta))}{r^3}, \tag{1}$$

where

$$\delta\omega = \gamma B_0 \frac{\Delta\chi}{3} \tag{2}$$

denotes the dipole field strength and γ is the gyromagnetic ratio. The polar angle between the external magnetic field and the position vector is denoted as θ as visualized in Fig. 1(c). The radius of the alveoli is denoted as R_A, and $P_2(x) = 3x^2/2 - 1/2$ is the Legendre polynomial with index 2. In general, spin-bearing particles experience a local Larmor frequency that depends on the geometrical

* Corresponding author at: German Cancer Research Center - DKFZ, Im Neuenheimer Feld 280, 69120 Heidelberg, Germany.
E-mail address: l.buschle@dkfz-heidelberg.de (L.R. Buschle).

https://doi.org/10.1016/j.jmr.2018.11.015
1090-7807/

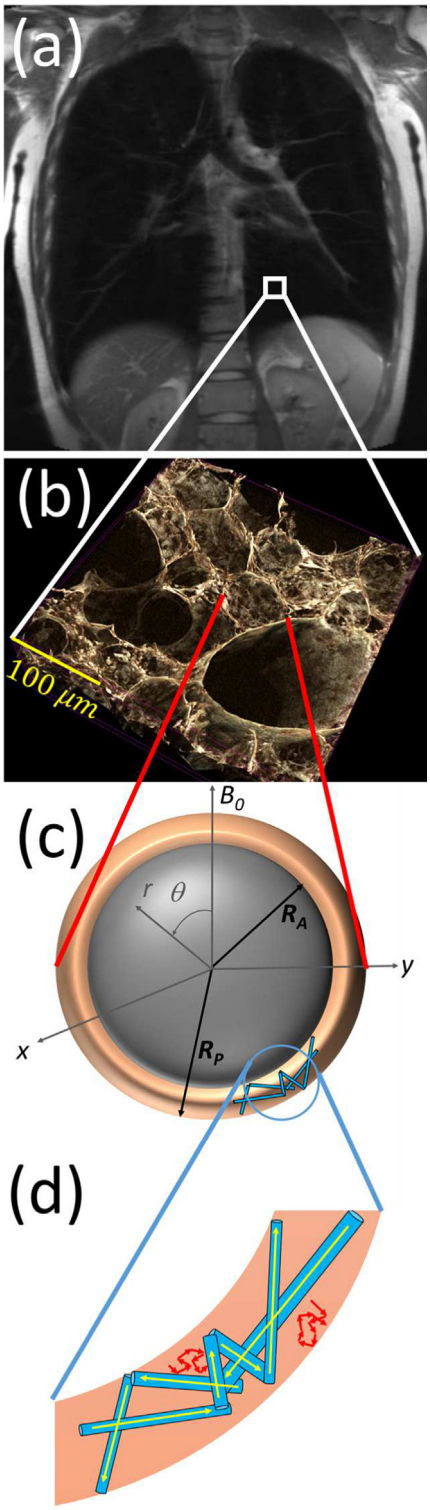

Fig. 1. Geometrical model of lung microstructure. The signal of the MR image (a) stems from the shown imaging voxel. Inside this voxel, the microscopic architecture of lung alveoli is visualized in (b) (μCT image from healthy mouse tissue; adapted from [9]) with field of view of 325 μm × 325 μm × 162.5 μm. A single alveolus is modelled as an air-filled sphere with radius R_A surrounded by a concentric sphere with radius R_P (c). Pseudo-diffusion effects (yellow arrows) as well as diffusion effects (red arrows) occur in the interstitial tissue surrounding the alveolus (d). (For interpretation of the references to colour in this figure legend, the reader is referred to the web version of this article.)

arrangements of all surrounding alveoli [11]. However, since the alveoli are densely packed in lung tissue, the contribution of outer alveoli is small since the average over the angular dependence of the three-dimensional dipole field is zero. Thus, only a single alveolus needs to be considered, as numerically demonstrated in [9].

Therefore, we only consider the signal evolution of the local magnetization around a single alveolus in the range $R_A \leqslant r \leqslant R_P$ and $0 \leqslant \theta < \pi$ between the inner alveolar radius R_A and outer perialveolar radius R_P, see Fig. 1(c). The mean ratio of the inner alveolar radii and outer perialveolar radii is connected to the mean air volume fraction η:

$$\eta = \frac{R_A^3}{R_P^3}. \tag{3}$$

It is advantageous to analyze the MR signal in dependence of the mean air volume fraction η, since it is macroscopically accessible, whereas the inner alveolar and the outer perialveolar radius show some variability in lung tissue. This model is well-established and is discussed in detail *e.g.* in [12–15].

In analogy to the intravoxel incoherent motion (IVIM), the blood flow in the microscopic capillaries around the alveoli can be considered as pseudo-diffusion [16]. Thus, the signal evolution is not only influenced by the susceptibility effects but also depends on diffusion and pseudo-diffusion of spin-bearing particles around the alveoli. Both effects are considered in the Bloch-Torrey-equation [17]. For the given form of the three-dimensional dipole field in Eq. (1), the Bloch-Torrey-equation could not yet be solved exactly; thus, approximative approaches had to be applied [18–20]. The alveolar surface model was introduced to allow an analytical treatment of both susceptibility and diffusion effects. In this model, the limit of large air volume fractions is assumed. Thus, spin-bearing molecules are mainly located on the surface of a spherical alveolus $r \approx R_A$, and the local Larmor frequency is given as:

$$\omega_{\text{surface}}(\theta) = \delta\omega\left[3\cos^2(\theta) - 1\right]. \tag{4}$$

This alveolar surface model has been analyzed extensively in [9], since this model allows an analytical solution of the Bloch-Torrey-equation.

In this work, we extend the alveolar surface model towards smaller air volume fractions with an improved approximation of the local Larmor frequency:

$$\omega(r,\theta) \approx \delta\omega R_A^2 \frac{3\cos^2(\theta) - 1}{r^2}, \tag{5}$$

for spin dephasing around an alveolus. This approximation is a natural improvement of the alveolar surface model. Specifically, the Larmor frequency of spin-bearing particles, that are not located on the surface of the alveoli, is much better described than in the alveolar surface model. In addition, this description also allows us to exactly solve the Bloch-Torrey equation and, thus, both free induction decay and corresponding lineshape can be obtained in dependence on microstructural parameters. Measurements of the MR signal and fitting routines then allow an estimation of these pathologically relevant parameters.

2. Material and methods

2.1. Pseudo-diffusion

The local magnetization $m(\mathbf{r}, t)$ is not only influenced by susceptibility effects, but also depends on motion effects of water molecules in the surrounding tissue. Especially the blood flow in capillaries around the alveoli shows no directional dependence (see Fig. 1(d)) and, thus, can be considered as pseudo-diffusion. This so-called intravoxel incoherent motion (IVIM) model is well-established in diffusion weighted imaging [16,21] and has also

been applied to lung MRI [22]. Pseudo-diffusion effects in lung MRI are also analyzed in [7,22]. While the classical IVIM concept considers the signal evolution for a Pulsed Field Gradient Spin Echo experiment, initially introduced by Stejskal and Tanner [23], the present scenario focuses on the simple free induction decay following an initial excitation pulse without any refocusing element. Thus, the strict distinction between coherent and incoherent dephasing effects becomes less important as no refocusing pulse is used. As the capillary vessels are more or less randomly distributed on the surface of the alveoli, an effective averaging process over all gradients and directions in the local off-resonance field is given. These circumstances allow replacing the ordinary diffusion process around an alveolus by a pseudo-diffusion process with an increased diffusion coefficient D^*, that considers the influence of perfusion on the free induction decay:

$$D^* = D + \frac{Lv}{6}, \tag{6}$$

where D denotes the diffusion coefficient, L is the mean capillary length (see Eq. (3) in [21]) and v the mean blood velocity in the capillaries. A rough approximation with $D \approx 1\ \mu m^2/ms$, mean capillary length $L \approx R_A \approx 100\ \mu m$ in the order of the alveolar radius, and a capillary flow velocity $v \approx 2\ \mu m/ms$ [21,24] show that the pseudo-diffusion coefficient is dominated by blood flow contributions in the order of $D^* \approx 35\ \mu m^2/ms$. To quantify the diffusion strength, it is convenient to introduce a pseudo-diffusion time:

$$\tau = \frac{R_A^2}{D^*}, \tag{7}$$

which is therefore in the order of $\tau \approx 300$ ms.

2.2. Time evolution of the magnetization

At the initial time point $t = 0$, the local magnetization is flipped into the transversal plane

$$m(\mathbf{r}, t = 0) = m_0 = \text{const.} \tag{8}$$

The local magnetization $m(\mathbf{r}, t) = m_x(\mathbf{r}, t) + \mathrm{i}m_y(\mathbf{r}, t)$ is then influenced by both susceptibility and diffusion effects. The time evolution of the local magnetization around an alveolus is governed by the Bloch-Torrey-equation [17]:

$$\frac{\partial}{\partial t} m(\mathbf{r}, t) = [D^* \Delta - \mathrm{i}\omega(\mathbf{r})] m(\mathbf{r}, t), \tag{9}$$

where the Laplace operator Δ in spherical coordinates is given as:

$$\Delta = \Delta_r + \frac{1}{r^2}\Delta_\theta \tag{10}$$

$$\Delta_r = \frac{\partial^2}{\partial r^2} + \frac{2}{r}\frac{\partial}{\partial r} \tag{11}$$

$$\Delta_\theta = \frac{1}{\sin(\theta)}\left[\cos(\theta)\frac{\partial}{\partial\theta} + \sin(\theta)\frac{\partial^2}{\partial\theta^2}\right]. \tag{12}$$

With the substitution

$$\xi = \cos(\theta) \tag{13}$$

the Laplace operator can be written in the form

$$\Delta = \Delta_r + \frac{1}{r^2}\Delta_\xi \tag{14}$$

$$\Delta_\xi = \left[1 - \xi^2\right]\frac{\partial^2}{\partial\xi^2} - 2\xi\frac{\partial}{\partial\xi}. \tag{15}$$

The local magnetization obeys reflecting boundary conditions on both, the inner alveolar radius and the outer perialveolar radius:

$$\left.\frac{\partial m(r,\theta,t)}{\partial r}\right|_{r=R_A} = 0 = \left.\frac{\partial m(r,\theta,t)}{\partial r}\right|_{r=R_P}. \tag{16}$$

The local magnetization cannot be directly measured since the voxel size in MRI is much larger than the typical alveolar diameter in lung tissue. Instead, the measurable total magnetization $M(t)$ is a superposition of the local magnetization $m(\mathbf{r}, t)$ over the dephasing volume V:

$$M(t) = \int_V \mathrm{d}^3\mathbf{r}\, m(\mathbf{r}, t) \tag{17}$$

$$= \int_{R_A}^{R_P} \mathrm{d}r r^2 \int_0^\pi \mathrm{d}\theta \sin(\theta) \int_0^{2\pi} \mathrm{d}\phi\, m(r,\theta,t). \tag{18}$$

The initial total magnetization $M_0 = M(0)$ depends on the initial local magnetization m_0 and the voxel size:

$$M_0 = M(0) = m_0 \frac{4}{3}\pi\left[R_P^3 - R_A^3\right]. \tag{19}$$

To obtain an analytical expression for the magnetization, the Bloch-Torrey-equation in the extended alveolar surface model is solved with a separation ansatz in analogy to Eq. (6) in [25] or Eq. (6) in [26]:

$$m(\mathbf{r}, t) = m(r,\theta,t) = m_0 \sum_{m=0}^{\infty}\sum_{n=1}^{\infty} c_{nm} R_{nm}(r)\Theta_m(\theta)\mathrm{e}^{-\kappa_{nm}^2\frac{t}{\tau}}. \tag{20}$$

In the following two subsections, the polar eigenfunctions $\Theta_m(\theta)$ and the radial eigenfunction $R_{nm}(r)$, as well as the respective eigenvalues κ_{nm}, and expansion coefficients c_{nm} will be analyzed.

2.3. Polar eigensystem

The separation of the polar part $\Theta_m(\theta)$ leads to an ordinary differential equation:

$$\left[\Delta_\theta - \mathrm{i}\tau\delta\omega\left[3\cos^2(\theta) - 1\right]\right]\Theta_m(\theta) = k_m[k_m + 1]\Theta_m(\theta), \tag{21}$$

with the separation constants $k_m[k_m + 1]$. With the abbreviation $\xi = \cos(\theta)$, this equation transforms into a spheroidal differential equation [27]:

$$\left[\Delta_\xi + \underbrace{k_m[k_m + 1] - 2\mathrm{i}\tau\delta\omega}_{\equiv\lambda_{2m,0}\left(\frac{1+\mathrm{i}}{2}\sqrt{6\tau\delta\omega}\right)} + 3\mathrm{i}\tau\delta\omega\left[1 - \xi^2\right]\right]\Theta_m(\xi) = 0, \tag{22}$$

where $\lambda_{2m,0}$ are the so-called spheroidal eigenvalues, which, in this special case, depend on the complex value $\sqrt{3\mathrm{i}\tau\delta\omega} = \frac{1+\mathrm{i}}{2}\sqrt{6\tau\delta\omega}$. The dependence of the complex eigenvalues $\lambda_{2m,0}$ on the purely real parameter $\tau\delta\omega$ is visualized in Fig. 6 in [9]. Due to the symmetry of the dipole field $\omega(r,\theta) = \omega(r, \pi - \theta)$ given in Eq. (5) and the symmetry of the spheroidal eigenfunctions $\mathrm{PS}_{l,0}(\cos(\theta)) = [-1]^l \mathrm{PS}_{l,0}(\cos(\pi - \theta))$, only the spheroidal eigenfunctions and eigenvalues with even indices $2m$ contribute to the polar eigenvalues and polar eigenfunctions:

$$k_m = -\frac{1}{2} + \sqrt{\frac{1}{4} + 2\mathrm{i}\tau\delta\omega + \lambda_{2m,0}\left(\frac{1+\mathrm{i}}{2}\sqrt{6\tau\delta\omega}\right)} \tag{23}$$

$$\Theta_m(\theta) = \mathrm{PS}_{2m,0}\left(\frac{1+\mathrm{i}}{2}\sqrt{6\tau\delta\omega}, \cos(\theta)\right), \tag{24}$$

where $\mathrm{PS}_{2m,0}\left(\frac{1+\mathrm{i}}{2}\sqrt{6\tau\delta\omega}, \cos(\theta)\right)$ are spheroidal eigenfunctions and $\lambda_{2m,0}\left(\frac{1+\mathrm{i}}{2}\sqrt{6\tau\delta\omega}\right)$ the corresponding eigenvalues. The underbraced term in Eq. (22) yields a quadratic equation for the polar eigenvalues k_m, which in general exhibits two solutions with different signs in front of the square root in Eq. (23). In the following analysis, the polar values will become indices of the radial eigenfunctions, which are linear combinations of spherical Bessel functions (see next subsection). Due to general properties of the linear combination of

spherical Bessel functions, given in Eq. (83) in [28], both solutions (with different signs in front of the square root in Eq. (23)) lead to the same radial eigenfunctions and, according to Eq. (79) in [28], to the same radial eigenvalues. Therefore, both solutions are linearly dependent and it is sufficient to focus on the solution given in Eq. (23). In the limit $\tau\delta\omega \to 0$, that corresponds to the motional-narrowing-regime, the spheroidal differential Eq. (22) becomes a Legendre differential equation and the polar eigenvalues become even numbers $\lim_{\tau\delta\omega\to 0} k_m = 2m$ by choosing the appropriate solution of the quadratic equation determined by the underbraced term in Eq. (22). Spheroidal eigenvalues and eigenfunctions for complex parameters are analyzed in detail in [27,29–32]. Fig. 2 shows the polar eigenvalues k_m in dependence on the parameter $\tau\delta\omega$.

2.4. Radial eigensystem

The radial part of the separation ansatz given in Eq. (20) yields a spherical Bessel differential equation for the radial eigenfunctions $R_{nm}(r)$ and the radial eigenvalues κ_{nm}:

$$r^2\left[\Delta_r + \frac{\kappa_{nm}^2}{R_A^2}\right]R_{nm}(r) = k_m[k_m+1]R_{nm}(r). \tag{25}$$

The radial eigenfunctions are a linear combination of spherical Bessel functions of the first and second kind j_{k_m}, y_{k_m}:

$$R_{nm}(r) = y'_{k_m}(\kappa_{nm})j_{k_m}\left(\kappa_{nm}\frac{r}{R_A}\right) - j'_{k_m}(\kappa_{nm})y_{k_m}\left(\kappa_{nm}\frac{r}{R_A}\right). \tag{26}$$

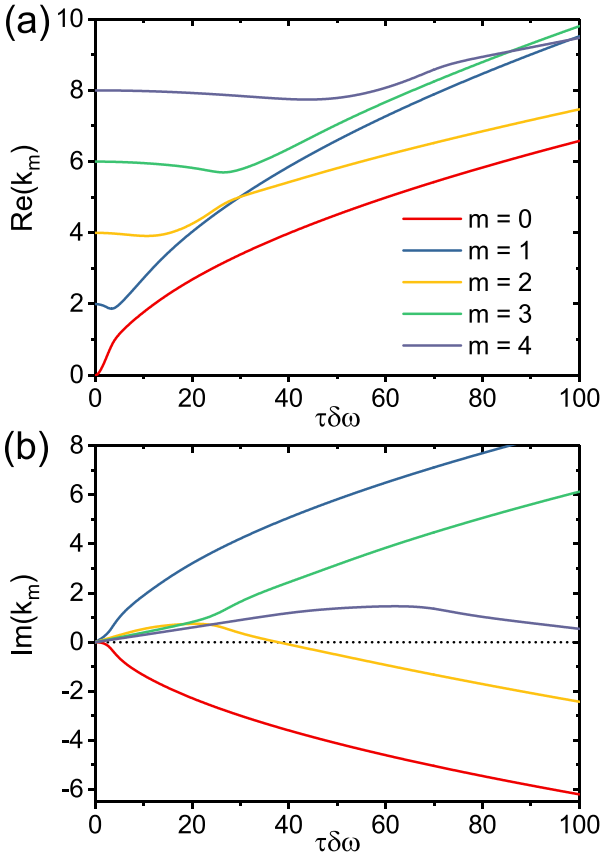

Fig. 2. Real part (a) and imaginary part (b) of the polar eigenvalues k_m in dependence on the parameter $\tau\delta\omega$, obtained from Eq. (23).

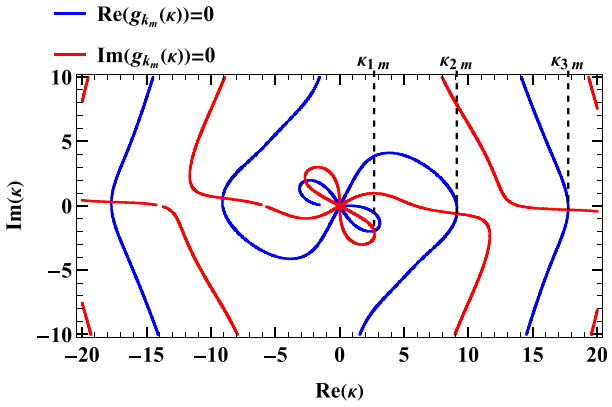

Fig. 3. Determination of the radial eigenvalues κ_{nm} as intersection of $\mathrm{Re}(g_{k_m}(\kappa)) = 0$ (blue lines) and $\mathrm{Im}(g_{k_m}(\kappa)) = 0$ (red lines) in the complex κ-plane (shown for $m = 0, \eta = 0.4, \tau\delta\omega = 20$, corresponding to $\lambda_{0,0}\left([1+\mathrm{i}]\sqrt{30}\right) = 4.71157 - 54.4997\mathrm{i}$ and $k_0 = 2.68486 - 2.27635\mathrm{i}$). (For interpretation of the references to colour in this figure legend, the reader is referred to the web version of this article.)

Evidently, these eigenfunctions obey the reflecting boundary conditions on the surface of the alveolus (see left hand side of Eq. (16)). The radial eigenvalues κ_{nm} are determined by the reflecting boundary condition on the outer perialveolar surface:

$$g_{k_m}(\kappa_{nm}) = 0 \tag{27}$$

$$g_{k_m}(\kappa) \equiv y'_{k_m}(\kappa)j'_{k_m}\left(\frac{\kappa}{\sqrt[3]{\eta}}\right) - j'_{k_m}(\kappa)y'_{k_m}\left(\frac{\kappa}{\sqrt[3]{\eta}}\right). \tag{28}$$

It is obvious from Eq. (79) in [28] that the other solution of the quadratic equation of the angular eigenvalues k_m given by Eq. (22) would lead to the same radial eigenvalues κ_{nm}. To obtain the radial eigenvalues κ_{nm}, the function $g_{k_m}(\kappa)$ will be analyzed in the complex κ-plane (see Fig. 3). For every complex-valued index k_m, the eigenvalues κ_{nm} can be obtained as intersections between curves with $\mathrm{Re}(g_{k_m}(\kappa)) = 0$ and $\mathrm{Im}(g_{k_m}(\kappa)) = 0$. To obtain the eigenvalues κ_{nm} numerically, it is advantageous to consider a discretized version of the spherical Bessel differential equation as analyzed in Appendix B. The radial eigenvalues κ_{nm} are shown in Fig. 4 in dependence on the parameter $\tau\delta\omega$. The expansion coefficients c_{nm} are necessary to compute the local magnetization $m(r,\theta,t)$. They can be obtained by utilizing the local magnetization given in Eq. (20) at the initial time point $t = 0$ as detailed in Appendix A. They are given as:

$$c_{nm} = [4m+1][-1]^m \times \frac{M_{nm}}{N_{nm}}\mathrm{PS}_{2m,0}\left(\frac{1+\mathrm{i}}{2}\sqrt{6\tau\delta\omega}, 0\right)\mathrm{S}^{(1)}_{2m,0}\left(\frac{1+\mathrm{i}}{2}\sqrt{6\tau\delta\omega}, 1\right), \tag{29}$$

where M_{nm} and N_{nm} are defined in Appendix A and $\mathrm{S}^{(1)}_{2m,0}$ denotes a radial prolate spheroidal function of the first kind. The expansion coefficients c_{nm} are visualized in Fig. 5 in dependence on the parameter $\tau\delta\omega$. Finally, the local magnetization $m(r,\theta,t)$ can be calculated according to Eq. (20).

3. Results

3.1. Total magnetization

As given in Eq. (17), the total magnetization $M(t)$ is a superposition of the local magnetization $m(\mathbf{r},t)$:

$$M(t) = M_0\sum_{n=1}^{\infty}\sum_{m=0}^{\infty} d_{nm}\mathrm{e}^{-\kappa_{nm}^2\frac{t}{\tau}} \tag{30}$$

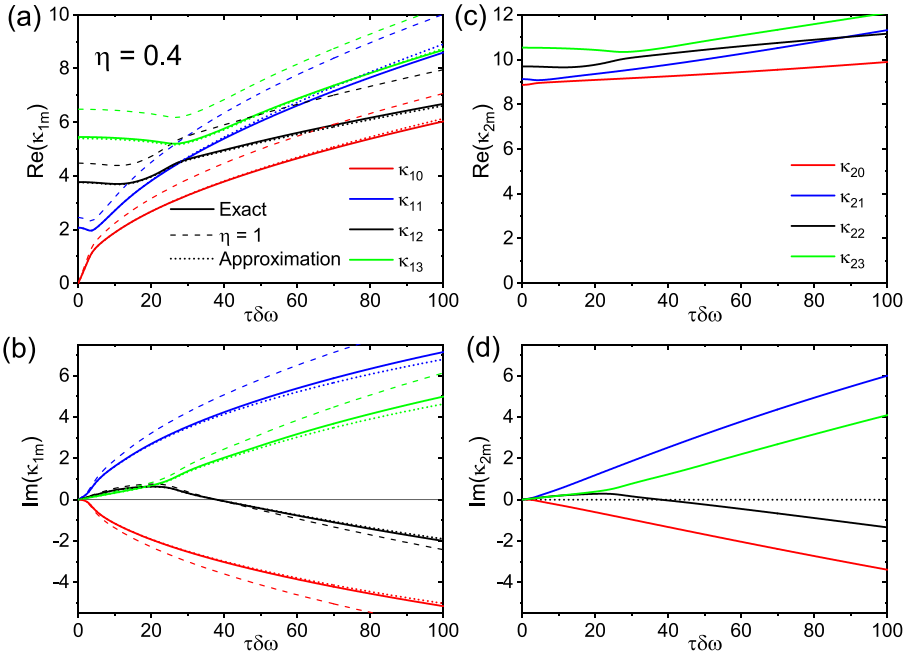

Fig. 4. Real part (a,c) and imaginary part (b,d) of the radial eigenvalues κ_{nm} in dependence of the parameter $\tau\delta\omega$ obtained from Eq. (27) for $\eta = 0.4$. (a,b) The dashed lines show the limit for $\eta \to 1$ from Eq. (36). The dotted lines show the approximations from Eq. (35).

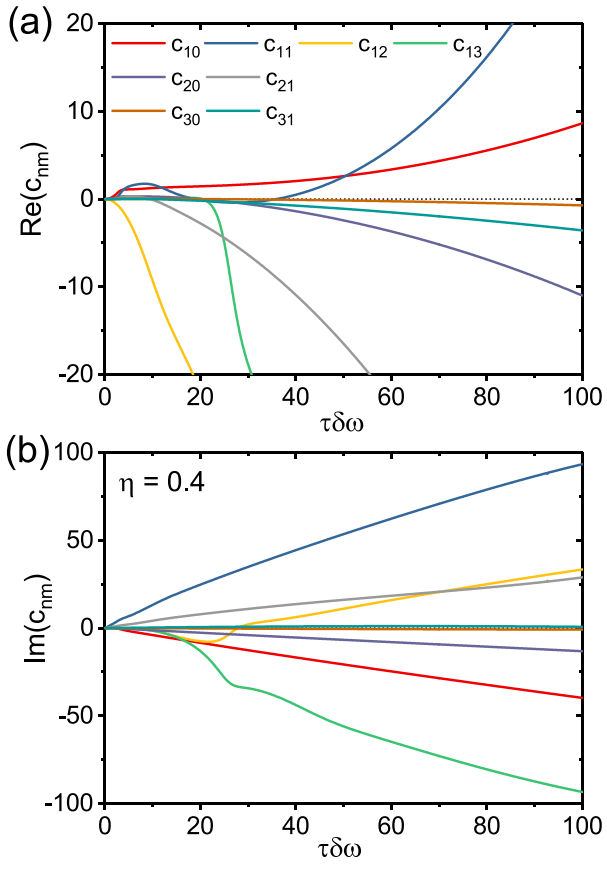

Fig. 5. Real part (a) and imaginary part (b) of the expansion coefficients c_{nm} in dependence of the parameter $\tau\delta\omega$ obtained from Eq. (29) for $\eta = 0.4$.

with the expansion coefficients d_{nm}:

$$d_{nm} = \frac{3\eta}{1-\eta}\frac{c_{nm}^2 N_{nm}}{4m+1} = \frac{3\eta}{1-\eta}\frac{M_{nm}^2}{N_{nm}}[4m+1] \times \left[\mathrm{PS}_{2m,0}\left(\frac{1+\mathrm{i}}{2}\sqrt{6\tau\delta\omega},0\right)\mathrm{S}_{2m,0}^{(1)}\left(\frac{1+\mathrm{i}}{2}\sqrt{6\tau\delta\omega},1\right)\right]^2, \quad (31)$$

where N_{nm} and M_{nm} are given in Appendix A in Eqs. (A4) and (A8). Evaluating the total magnetization in Eq. (30) at $t = 0$, the coefficients d_{nm} exhibit the relation

$$\sum_{n=1}^{\infty}\sum_{m=0}^{\infty} d_{nm} = 1, \quad (32)$$

which can be used to estimate the number of required coefficients for sufficient numerical accuracy. The total magnetization only depends on the coefficients d_{nm} and the radial eigenvalues κ_{nm}, that are defined by Eq. (27), and can be numerically calculated as shown in Appendix B.

3.2. Large air volume fraction

For large air volume fractions $\eta \to 1$, the coefficients d_{nm} become

$$\lim_{\eta\to 1} d_{nm} = \delta_{1n}[4m+1]\left[\mathrm{PS}_{2m,0}\left(\frac{1+\mathrm{i}}{2}\sqrt{6\tau\delta\omega},0\right)\mathrm{S}_{2m,0}^{(1)}\left(\frac{1+\mathrm{i}}{2}\sqrt{6\tau\delta\omega},1\right)\right]^2, \quad (33)$$

where we used the limit

$$\lim_{\eta\to 1}\frac{3\eta}{1-\eta}\frac{M_{nm}^2}{N_{nm}} = \delta_{n1} \quad \text{for all } m. \quad (34)$$

The coefficients d_{1m} corresponds to the expansion coefficients in Eq. (21) in [9]. The coefficients d_{nm} are shown in Fig. 6 for large air volume fractions η in dependence on the parameter $\tau\delta\omega$.

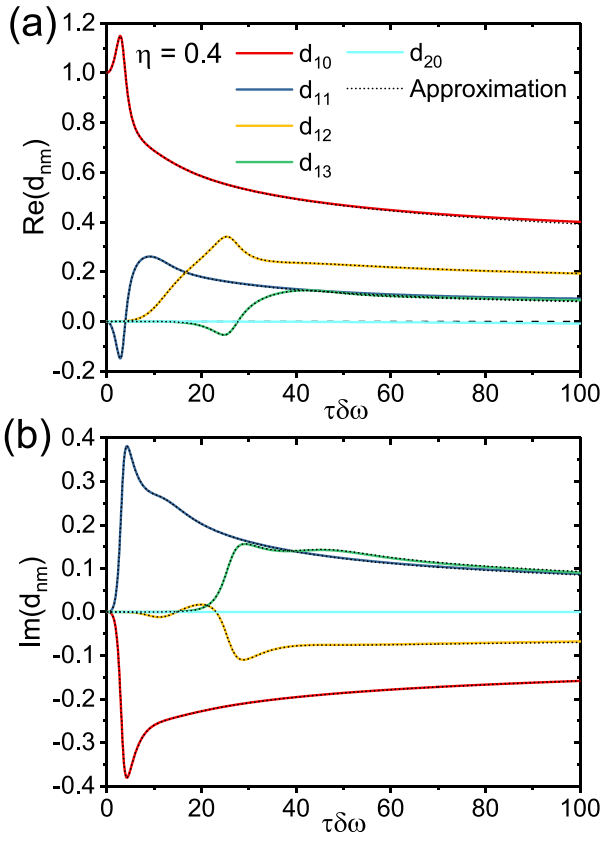

Fig. 6. Real part (a) and imaginary part (b) of the expansion coefficients d_{nm} in dependence of the parameter $\tau\delta\omega$ obtained from Eq. (31) for $\eta = 0.4$. The dotted line shows the approximation from Eq. (33). According to Eq. (32), the sum of all the real part of the coefficients d_{nm} takes the value of 1 for all possible parameters of $\tau\delta\omega$, whereas the sum of the imaginary parts vanishes.

The eigenvalues κ_{1m} for large air volume fractions can be obtained from Eq. (90) in [28] or Eq. (34) in [33]:

$$\kappa_{1m} \approx \sqrt{k_m[1+k_m]}\sqrt{2-\eta^{-\frac{1}{3}}+\frac{2}{3}\left[1-\eta^{-\frac{1}{3}}\right]^2+\frac{1}{3}\left[1-\eta^{-\frac{1}{3}}\right]^3+\left[\frac{1}{9}-k_m\frac{1+k_m}{30}\right]\left[1-\eta^{-\frac{1}{3}}\right]^4}. \tag{35}$$

In the limit $\eta \to 1$, the eigenvalues κ_{1m}^2 coincide with the eigenvalues given in Eq. (19) in [9]:

$$\kappa_{1m} = \sqrt{k_m[k_m+1]} = \sqrt{\lambda_{2m,0}\left(\frac{1+\mathrm{i}}{2}\sqrt{6\tau\delta\omega}\right)+2\mathrm{i}\tau\delta\omega}. \tag{36}$$

The eigenvalues κ_{1m} and their limits for large η are shown in Fig. 4 in dependence on the parameter $\tau\delta\omega$. Thus, the magnetization $M(t)$ can be obtained for large air volume fractions η as:

$$M(t) = M_0\sum_{m=0}^{\infty} d_{1m}\mathrm{e}^{-\kappa_{1m}^2\frac{t}{\tau}}. \tag{37}$$

3.3. Lineshape

In the limit of static dephasing, the lineshape $p(\omega)$ gives the probability of finding a specific Larmor frequency ω inside a voxel. Usually, this lineshape is obtained from a histogram analysis of the Larmor frequency and, thus, is obviously purely real (see chapter 6 in [34]). However, in the presence of diffusion, the lineshape represents the Fourier transform of the free induction decay:

$$p(\omega) = \frac{1}{2\pi}\int_{-\infty}^{+\infty}\frac{M(t)}{M_0}\mathrm{e}^{+\mathrm{i}\omega t}\mathrm{d}t. \tag{38}$$

In general, this lineshape is not necessarily real but exhibits an imaginary part known as dispersion. In MR spectroscopy, however, the lineshape is typically phased, which means that real and imaginary part of the lineshape are combined to a purely real lineshape, see *e.g.* Chapter 3 in [35] or [36]. These phased lineshapes agree with purely real lineshapes that assume the time symmetry $M(-t) = M^*(t)$ for negative times:

$$p(\omega) = \frac{1}{\pi}\int_0^{\infty}\mathrm{d}t\mathrm{Re}\left(\mathrm{e}^{\mathrm{i}\omega t}\frac{M(t)}{M_0}\right). \tag{39}$$

It is therefore advantageous to consider only the purely real lineshape, since the magnetization decay exhibits real and imaginary parts corresponding to the transverse components $\mathrm{Re}(M(t)) = M_x(t)$ and $\mathrm{Im}(M(t)) = M_y(t)$. The magnetization can be obtained as the inverse Fourier transform of the lineshape:

$$\frac{M(t)}{M_0} = \int_{-\infty}^{+\infty} p(\omega)\mathrm{e}^{-\mathrm{i}\omega t}\mathrm{d}\omega. \tag{40}$$

Applying Eq. (39) to the total magnetization, given in Eq. (30), the lineshape can be obtained as:

$$p(\omega) = \frac{\tau}{\pi}\sum_{n=1}^{\infty}\sum_{m=0}^{\infty}\mathrm{Re}\left(\frac{d_{nm}}{\kappa_{nm}^2-\mathrm{i}\tau\omega}\right) \tag{41}$$

$$= \frac{\tau}{\pi}\sum_{n=1}^{\infty}\sum_{m=0}^{\infty}\frac{\mathrm{Re}\left(d_{nm}\kappa_{nm}^{2*}\right)-\tau\omega\mathrm{Im}(d_{nm})}{|\kappa_{nm}|^4-2\tau\omega\mathrm{Im}\left(\kappa_{nm}^2\right)+[\tau\omega]^2}. \tag{42}$$

In the static dephasing limit, where diffusion is neglected, the lineshape in the extended alveolar surface model is given as:

$$p_{\mathrm{SD}}(\omega) = \frac{\eta}{1-\eta}\frac{3\sqrt{3}}{16}\frac{\delta\omega}{\omega^2}\left[\left[1-\frac{2}{3}\frac{\omega}{\delta\omega}\right]\sqrt{1+\frac{\omega}{\delta\omega}}+f\left(\frac{\omega}{\delta\omega}\right)\right], \tag{43}$$

where the function $f(\omega/\delta\omega)$ can be found as:

$$f\left(\frac{\omega}{\delta\omega}\right) = \begin{cases} \sqrt{-\frac{\delta\omega}{\omega}}\left[\frac{\pi}{2}-\arcsin\left(\sqrt{-\frac{\omega}{\delta\omega}}\right)\right] & \text{for} \quad -1 \leqslant \frac{\omega}{\delta\omega} \leqslant -\eta^{\frac{2}{3}} \\ \left[\frac{1}{\eta}\frac{2}{3}\frac{\omega}{\delta\omega}-\frac{1}{\sqrt[3]{\eta}}\right]\sqrt{1+\eta^{-\frac{2}{3}}\frac{\omega}{\delta\omega}} & \text{for} \quad -\eta^{\frac{2}{3}} \leqslant \frac{\omega}{\delta\omega} \leqslant 2\eta^{\frac{2}{3}} \\ +\sqrt{\frac{\delta\omega}{\omega}}\ln\left(\frac{\eta^{-\frac{1}{3}}+\sqrt{\eta^{-\frac{2}{3}}+\frac{\delta\omega}{\omega}}}{1+\sqrt{1+\frac{\delta\omega}{\omega}}}\right) & \\ \sqrt{\frac{\delta\omega}{\omega}}\left[\frac{\sqrt{6}}{3}+\ln\left(\sqrt{\frac{\delta\omega}{\omega}}\frac{\sqrt{2}+\sqrt{3}}{1+\sqrt{1+\frac{\delta\omega}{\omega}}}\right)\right] & \text{for} \quad 2\eta^{\frac{2}{3}} \leqslant \frac{\omega}{\delta\omega} \leqslant 2. \end{cases} \tag{44}$$

Details about the derivation of this equation are provided in Appendix C.

In the limit $\eta \to 1$, the lineshape becomes

$$\lim_{\eta\to 1} p_{\mathrm{SD}}(\omega) = \frac{1}{2\delta\omega\sqrt{3\left[1+\frac{\omega}{\delta\omega}\right]}} \quad \text{for} \quad -1 < \frac{\omega}{\delta\omega} < +2, \tag{45}$$

which agrees with the alveolar surface model obtained in Eq. (13) in [9]. In Fig. 7, the lineshape in the extended alveolar surface model is compared with random walk simulations of the exact dipole field as described in Eq. (1). Details of the random walk algorithm are provided in [37]. The diffusion time τ is governed by the pseudo-diffusion coefficient (see Eq. (7)) and the lineshape $p(\omega)$ depends only on the product $\tau\delta\omega$, due to the scaling laws of this problem [38]. The lineshape of the extended alveolar surface model shows a better agreement for the given parameters η and $\tau\delta\omega$ than the static dephasing lineshape, given in Eq. (43), and the lineshape obtained from the alveolar surface model (see Eq. (41) with d_{nm} given in Eq. (33) and κ_{1m} given in Eq. (36)).

In MR imaging, the signal evolution is often described as a monoexponential decrease with an offset frequency $M(t) = \mathrm{e}^{-R_2't-\mathrm{i}\Phi t}$. A mean relaxation time approach allows determin-

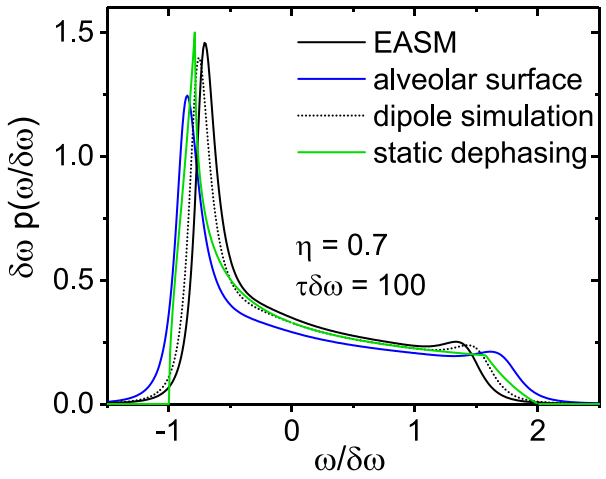

Fig. 7. Comparison between lineshapes $p(\omega)$ in the extended alveolar surface model (EASM) (Eq. (41)), the alveolar surface model (see Eq. (41) with d_{nm}, given in Eq. (33), and κ_{1m}, given in Eq. (36)) and the static dephasing lineshape (Eq. (43)). The extended alveolar surface model shows the best agreement to random walk simulations for the exact dipole field.

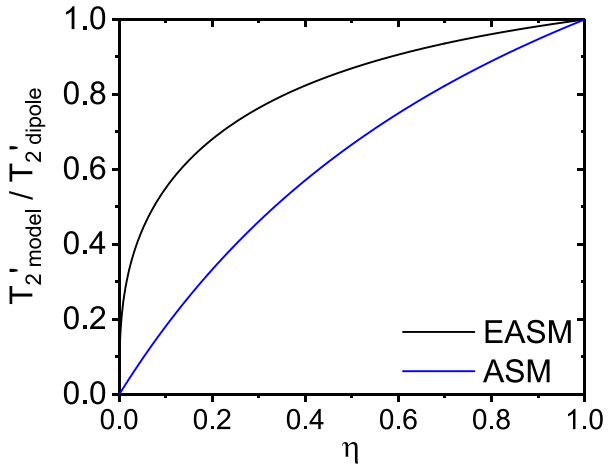

Fig. 8. Ratio of static dephasing relaxation times for the extended alveolar surface model (EASM) and the exact dipole field $T'_{2\text{EASM}}/T'_{2\text{dipole}}$ as given in Eq. (52). For physiological air volume fractions $\eta > 0.6$, the deviation of both relaxation times is smaller than 10%. Particularly, the extended alveolar surface model is a better description than the alveolar surface model (ASM) given by Eq. (51).

ing the monoexponential relaxation rate $R'_2 = 1/T'_2$, and the offset frequency Φ:

$$\frac{1}{R'_{2\text{EASM}} + \mathrm{i}\Phi_{\text{EASM}}} = \int_0^\infty \mathrm{d}t \frac{M_{\text{SD}}(t)}{M_0} \tag{46}$$

$$= \pi p_{\text{SD}}(0) - \mathrm{i}\int_{-\infty}^{+\infty} \mathrm{d}\omega \frac{p_{\text{SD}}(\omega)}{\omega} \tag{47}$$

$$= \frac{1}{V}\int_V \mathrm{d}^3\mathbf{r}\left[\pi\delta(\omega(\mathbf{r})) + \frac{\mathrm{i}}{\omega(\mathbf{r})}\right] \tag{48}$$

$$= \frac{\sqrt{3}}{10}\frac{\eta}{\delta\omega}\frac{\eta^{-5/3}-1}{1-\eta}\left[\pi + 2\mathrm{i}\,\text{arccoth}\left(\sqrt{3}\right)\right]. \tag{49}$$

The R'_2 relaxation time in the extended alveolar surface model is larger than for the exact dipole field:

$$\frac{1}{R'_{2\text{dipole}} + \mathrm{i}\Phi_{\text{dipole}}} = \frac{1+\eta}{\eta\delta\omega}\frac{1}{4\sqrt{3}}\left[\pi + 2\mathrm{i}\,\text{arccoth}\left(\sqrt{3}\right)\right]. \tag{50}$$

In the alveolar surface model ($\eta \to 1$), the relaxation rates and phases of both models (Eqs. (49) and (50)) converge to the same limit

$$\frac{1}{R'_{2\text{surface}} + \mathrm{i}\Phi_{\text{surface}}} = \frac{1}{2\sqrt{3}\delta\omega}\left[\pi + 2\mathrm{i}\,\text{arccoth}\left(\sqrt{3}\right)\right]. \tag{51}$$

Interestingly, the ratio of the relaxation rates $R'_{2\text{dipole}}/R'_{2\text{EASM}}$ only depends on air volume fraction η, and is equal to the ratio of the offset phases:

$$\frac{T'_{2\text{EASM}}}{T'_{2\text{dipole}}} = \frac{R'_{2\text{dipole}}}{R'_{2\text{EASM}}} = \frac{\Phi_{\text{dipole}}}{\Phi_{\text{EASM}}} = \frac{6}{5}\frac{\eta^{1/3}-\eta^2}{1-\eta^2}. \tag{52}$$

The ratio of the relaxation times is shown in Fig. 8 in dependence on air volume fraction η.

3.4. Application to lung tissue

A healthy volunteer was studied under the supervision of a board-certified radiologist. All images were acquired with a Magnetom Aera 1.5T (Siemens Healthcare, Erlangen, Germany). Approval for data collection and the study protocol was given by the institutional review board of the medical faculty. Informed consent for study inclusion was obtained from the volunteer. A cubic 15 mm × 15 mm × 15 mm voxel as visualized in Fig. 1(a) was selected to acquire the free induction decay in expiration using the PRESS sequence [39,40] with TR = 1.5 s, echo time TE = 30 ms and twenty averages (NA = 20). The location and the size of the voxel were chosen in such a way that influences and artifacts of the surrounding tissue boundaries were minimized. The measured lineshape is compared with the theoretical lineshape, given in Eq. (38), for realistic values of the dipole field strength $\delta\omega$, the air volume fraction η, and the diffusion time τ, that are Gaussian distributed. The susceptibility difference between air and soft tissue is approximatively $\Delta\chi = 9.4$ ppm, the susceptibility difference between air and deoxygenized blood is $\Delta\chi = 6.9$ ppm [41]. According to Eq. (2), this yields a Gaussian distributed dipole field strength with mean value and standard deviation $\delta\omega = 0.9\,\text{kHz} \pm 0.3\,\text{kHz}$. The air volume fraction, even in expiration, is very high with $\eta \approx 0.7 \pm 0.1$ [9,42], and the diffusion time τ can roughly be estimated with $R_A \approx 100\mu$m [43] and $v \approx 2\,\mu$m/ms [21,24] as $\tau \approx 300\,\text{ms} \pm 100\,\text{ms}$. The lineshape $p(\omega)$ in the extended alveolar surface model is given in Eq. (41) and the lineshape $p_{\text{SD}}(\omega)$ in the alveolar surface model is given in Eq. (43). In Fig. 9, both lineshapes are compared with the measured lineshape in healthy human lung tissue. However, since physiological tissue shows some variability, we assumed a Gaussian distribution of the underlying parameters. Finally, the theoretical lineshapes are given as:

$$p(\omega) = \frac{1}{[2\pi]^{3/2}}\int_{-\infty}^{+\infty}\mathrm{d}\delta\omega\int_{-\infty}^{+\infty}\mathrm{d}\eta \int_{-\infty}^{+\infty}\mathrm{d}\tau \mathrm{e}^{-\frac{[\delta\omega-\delta\omega_{\text{mean}}]^2}{2\delta\omega^2_{\text{std}}}}\mathrm{e}^{-\frac{[\eta-\eta_{\text{mean}}]^2}{2\eta^2_{\text{std}}}}\mathrm{e}^{-\frac{[\tau-\tau_{\text{mean}}]^2}{2\tau^2_{\text{std}}}}p(\omega,|\delta\omega|,|\eta|,|\tau|), \tag{53}$$

where $\delta\omega = 0.9\,\text{kHz} \pm 0.3\,\text{kHz}, \tau = 300\,\text{ms} \pm 50\,\text{ms}$ and $\eta = 0.7 \pm 0.1$ are assumed. The measured and theoretical lineshapes are compared in Fig. 9.

4. Discussion and conclusion

Lung tissue consists of densely packed alveoli that are surrounded by small capillaries [44,45]. In MR imaging, the susceptibility difference between air and tissue causes a fast decay of the magnetization. In previous works, this free induction decay from a single spherical alveolus could be analyzed in detail [12]. However, this model does not allow solving the Bloch-Torrey equation

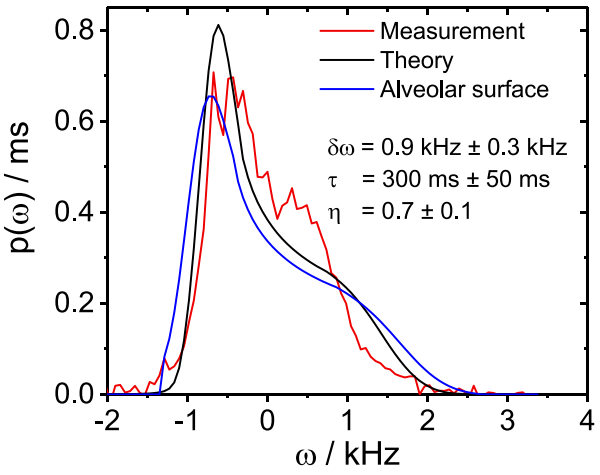

Fig. 9. Comparison of the measured lineshape (red line) and the lineshape of the extended alveolar surface model (black line) as well as the previously used alveolar surface model (blue line). We assume typical physiological Gaussian distributed values of the dipole field strength $\delta\omega$, the air volume fraction η, and the pseudo-diffusion time τ. The measured lineshape was obtained as a PRESS measurement in expiration in a healthy volunteer. (For interpretation of the references to colour in this figure legend, the reader is referred to the web version of this article.)

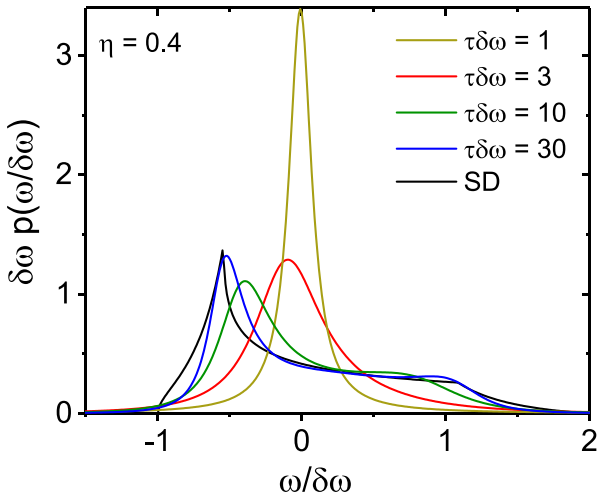

Fig. 10. Lineshape $p(\omega)$ obtained from Eq. (41) in dependence on the parameter $\tau\delta\omega$. For strong diffusion effects (small $\tau\delta\omega$), the lineshape is nearly Lorentzian-shaped and symmetric. With increasing values of the parameter $\tau\delta\omega$, the width increases and the peak is shifted to the left. For large $\tau\delta\omega$, the specific peak structure occurs. The static dephasing (SD) limit is given in Eq. (43).

and, thus, cannot account for a complete description of diffusion and pseudo-diffusion effects. The movement of spin-bearing particles in interstitial lung tissue around alveoli is mainly influenced by two components: the free diffusion around the alveoli and the microcirculation of blood in the capillaries that surround the alveoli. While the free diffusion is restricted by boundaries of the interstitial tissue, it is necessary to incorporate the motion of spin-bearing particles in interstitial tissue to a so-called pseudo-diffusion process. This approach resembles the well-known pseudo-diffusion process for describing intravoxel incoherent motion (IVIM) as proposed by Le Bihan [16,21]. In general, spins diffuse with different pseudo-diffusion coefficients D^*, which results in a non-trivial distribution of the pseudo-diffusion time τ. In this work, we assume a Gaussian distribution of the pseudo-diffusion time in Fig. 9; however, this model can easily be generalized to arbitrary pseudo-diffusion time distributions that *e.g.* describe different tissue compartments.

Since the Bloch-Torrey equation is not solvable for a single spherical alveolus, one needs to apply approximative methods such as the strong collision approximation [20,46,47] or the weak field approximation [18]. The free induction decay could only be solved exactly in the limit of very large air volume fractions $\eta \to 1$, in the so-called alveolar surface model [9].

In this work, the alveolar surface model is extended towards smaller air volume fractions η by an approximation of the three-dimensional dipole field. The advantage of choosing the modified Larmor frequency, as given in Eq. (5), is that the Bloch-Torrey equation can be solved exactly, and the results are also approximately valid for smaller air volume fractions. In fact, the Larmor frequency at $r = R_P$ is only overestimated by a factor of $1/\eta^{1/3}$. Thus, for $\eta = 0.5$ the alveolar surface model overestimates the local Larmor frequency on the outer perialveolar by a factor of 2, whereas the extended alveolar surface model overestimates the Larmor frequency only by a factor of 1.26.

The Bloch-Torrey equation is solved by a separation ansatz, revealing a spheroidal differential equation for the polar eigensystem and a Bessel differential equation for the radial eigensystem. The obtained lineshapes highly depend on the influence of diffusion effects, see Fig. 10: for large diffusion effects, the lineshape is symmetric and nearly Lorentzian-shaped, whereas for small diffusion effects, the lineshape shows a strong asymmetry with two prominent peaks.

When compared with the alveolar surface model, where dephasing is restricted to the surface of an alveolus, the presented model accounts for the more realistic scenario where radial diffusion and dephasing are incorporated. This results in a more realistic form of the lineshape: while the static dephasing lineshape in the alveolar surface model exhibits a continuous decrease in the interval $-\delta\omega < \omega < 2\delta\omega$ with artificial singularities on both boundaries, the lineshape in the presented model exhibits a more realistic form with continuous values at the boundaries of the frequency interval. This improvement is shown in Fig. 9, where the frequency distribution obtained in the extended alveolar surface model agrees better with measurements than the alveolar surface model.

For the exact dipole field with the inverse cubic radial dependence (see Eq. (1)), the diffusion process between the inner alveolar surface and the outer perialveolar surface could be analyzed in the strong collision approximation. This approach leads to a classification of the interplay between diffusion and susceptibility effects into different diffusion regimes as visualized in Fig. 3(b) in [20]. The free induction decay in the strong collision approximation depends on the underlying diffusion regime, which needs to be classified with the given pulmonary microstructural parameters. One advantage of the presented methods is the generalization of the signal formation for arbitrary microstructural parameters.

The lineshapes in the static dephasing regime of the exact dipole field and in the extended alveolar surface model agree very well, even in the case of relatively small air volume fractions. This can be confirmed by taking a monoexponential approximation of the free induction decay with relaxation time T_2'. As given in Eq. (52) and shown in Fig. 8, the relaxation times for the exact dipole field and the extended alveolar surface model differ only about 1.8% for $\eta = 0.9$ or 17.6% for $\eta = 0.4$ in the static dephasing limit. For non-vanishing diffusion effects, this difference would even be smaller.

Theoretical findings are compared with *in vivo* measurements in healthy human lung tissue by analyzing the water peak of a PRESS measurement. The measured lineshape agrees very well

with the theoretical lineshape for realistic values of the air volume fraction η, the susceptibility difference $\Delta\chi$ and the pseudo-diffusion time τ as shown in Fig. 9. For clinical application, this method should be extended by measuring lineshapes of different voxels to obtain parameter maps. Technically, this can be performed by using, *e.g.*, a motion-navigated chemical shift imaging (CSI) sequence.

In conclusion, this work presents a model for the signal decay in lung MRI under the influence of microscopic susceptibility and pseudo-diffusion effects. In contrast to the previously developed alveolar surface model, this model accounts for realistic air volume fractions. The obtained lineshapes agree very well with *in vivo* measurements. Hence, with sophisticated MR sequences, a mapping of microstructural lung parameters should be possible.

Acknowledgements

We thank D. A. Kann from Instituto de Astrofísica de Andalucía, Granada, Spain for proofreading of the manuscript. This work was supported by grants from the Deutsche Forschungsgemeinschaft (contract Grant No.: DFG ZI 1295/2-1 and DFG KU 3555/1-1). L. R. Buschle was supported by Studienstiftung des Deutschen Volkes.

Appendix A. Calculation of the expansion coefficients

The expansion coefficients c_{nm} are obtained by evaluating the ansatz (Eq. (20)) of the local magnetization at the initial time point $t = 0$:

$$1 = \sum_{m=0}^{\infty}\sum_{n=1}^{\infty} c_{nm} R_{nm}(r)\mathrm{PS}_{2m,0}\left(\frac{1+\mathrm{i}}{2}\sqrt{6\tau\delta\omega}, \cos(\theta)\right). \tag{A1}$$

As shown by Herberthson et al., the eigenfunctions of the Bloch-Torrey-operator are generally self-dual (see [48] and Lemma 1 in Appendix A in [49]). For the polar part, one finds the orthogonality relation [9,32]:

$$\int_0^{\pi} \mathrm{d}\theta \sin(\theta)\mathrm{PS}_{2m,0}\left(\frac{1+\mathrm{i}}{2}\sqrt{6\tau\delta\omega}, \cos(\theta)\right) \mathrm{PS}_{2m',0}\left(\frac{1+\mathrm{i}}{2}\sqrt{6\tau\delta\omega}, \cos(\theta)\right) = \frac{2}{4m+1}\delta_{mm'} \tag{A2}$$

and the orthogonality relation of the linear combination of the spherical Bessel functions for the radial part (see Eqs. (101) and (102) in [28])

$$\frac{1}{R_{\mathrm{A}}^3}\int_{R_{\mathrm{A}}}^{R_{\mathrm{P}}} \mathrm{d}r r^2 R_{nm}(r) R_{n'm}(r) = N_{nm}\delta_{nn'} \tag{A3}$$

$$N_{nm} = \frac{\sqrt[3]{\eta}}{2\kappa_{nm}^4}\left[\frac{j'_{k_m}(\kappa_{nm})}{j'_{k_m}\left(\frac{\kappa_{nm}}{\sqrt[3]{\eta}}\right)}\right]^2\left[1 - \frac{k_m[k_m+1]}{\kappa_{nm}^2}\eta^{\frac{2}{3}}\right] + \frac{1}{2\kappa_{nm}^4}\left[\frac{k_m[k_m+1]}{\kappa_{nm}^2} - 1\right]. \tag{A4}$$

Finally, one obtains the expansion coefficient c_{nm} as

$$c_{nm} = \frac{4m+1}{2N_{nm}}\int_0^{\pi} \mathrm{d}\theta \sin(\theta)\mathrm{PS}_{2m,0}\left(\frac{1+\mathrm{i}}{2}\sqrt{6\tau\delta\omega}, \cos(\theta)\right)\frac{1}{R_{\mathrm{A}}^3} \times \int_{R_{\mathrm{A}}}^{R_{\mathrm{P}}} \mathrm{d}r r^2 R_{nm}(r). \tag{A5}$$

The remaining integrals can be solved analytically: the integral of spheroidal functions reveals

$$\int_0^{\pi} \mathrm{d}\theta \sin(\theta)\mathrm{PS}_{2m,0}\left(\frac{1+\mathrm{i}}{2}\sqrt{6\tau\delta\omega}, \cos(\theta)\right) = 2[-1]^m \mathrm{PS}_{2m,0}\left(\frac{1+\mathrm{i}}{2}\sqrt{6\tau\delta\omega}, 0\right)\mathrm{S}_{2m,0}^{(1)}\left(\frac{1+\mathrm{i}}{2}\sqrt{6\tau\delta\omega}, 1\right) \tag{A6}$$

and the integral over spherical Bessel functions gives (see Eq. (103) in [28]):

$$\frac{1}{R_{\mathrm{A}}^3}\int_{R_{\mathrm{A}}}^{R_{\mathrm{P}}} \mathrm{d}r r^2 R_{nm}(r) = M_{nm} \tag{A7}$$

$$M_{nm} = \frac{k_m}{\kappa_{nm}^2}\sqrt{\eta}\frac{j'_{k_m}(\kappa_{nm})}{j'_{k_m}\left(\frac{\kappa_{nm}}{\sqrt[3]{\eta}}\right)}\left[s_{\frac{3}{2},k_m+\frac{1}{2}}\left(\frac{\kappa_{nm}}{\sqrt[3]{\eta}}\right) - \frac{\kappa_{nm}}{\sqrt[3]{\eta}}s_{\frac{1}{2},k_m+\frac{3}{2}}\left(\frac{\kappa_{nm}}{\sqrt[3]{\eta}}\right)\right] + \frac{k_m}{\kappa_{nm}^2}\left[\kappa_{nm}s_{\frac{1}{2},k_m+\frac{3}{2}}(\kappa_{nm}) - s_{\frac{3}{2},k_m+\frac{1}{2}}(\kappa_{nm})\right], \tag{A8}$$

with the Lommel function [50]

$$s_{\kappa,\nu}(z) = \frac{z^{\kappa+1}}{[\kappa+1]^2 - \nu^2}\,{}_1F_2\left(1; \frac{\kappa-\nu+3}{2}, \frac{\kappa+\nu+3}{2}; -\frac{z^2}{4}\right). \tag{A9}$$

The quotient $j'_{k_m}(\kappa_{nm})/j'_{k_m}(\kappa_{nm}/\sqrt[3]{\eta})$ in Eqs. (A4) and (A8) can be written with the Wronski determinant (see Eqs. (98) and (99) in [28]) as:

$$\frac{j'_{k_m}(\kappa_{nm})}{j'_{k_m}\left(\frac{\kappa_{nm}}{\sqrt[3]{\eta}}\right)} = \eta^{-\frac{2}{3}}\kappa_{nm}^2 R_{nm}(R_{\mathrm{P}}). \tag{A10}$$

Finally, the expansion coefficients c_{nm} are given in Eq. (29).

Appendix B. Numerical analysis of the radial eigensystem

For numerical determination of the radial eigenvalues κ_{nm} for given polar eigenvalues k_m, it is convenient to rewrite the spherical Bessel differential Eq. (25) in the form:

$$\left[\frac{2\mathrm{i}\tau\delta\omega + \lambda_{2m,0}\left(\frac{1+\mathrm{i}}{2}\sqrt{6\tau\delta\omega}\right)}{r^2} - \Delta_r\right]R_{nm}(r) = \left[\frac{k_m[k_m+1]}{r^2} - \Delta_r\right]R_{nm}(r) = \frac{\kappa_{nm}^2}{R_{\mathrm{A}}^2}R_{nm}(r). \tag{B1}$$

The radial interval $R_{\mathrm{A}} \leqslant r \leqslant R_{\mathrm{P}}$ can be discretized in the following form:

$$r_i = R_{\mathrm{A}} + [i-1]h \quad \text{for} \quad i = 1, \ldots, N \quad \text{with step size} \quad h = \frac{R_{\mathrm{P}} - R_{\mathrm{A}}}{N-1}. \tag{B2}$$

As shown in [51], the radial part of the three-dimensional Laplace operator can be written in the following matrix form (see also Eq. (94) in [28]):

$$\hat{\Delta}_r = \frac{1}{h^2}\begin{pmatrix} -2\frac{r_{1\frac{1}{2}}^2}{r_1^2} & +2\frac{r_{1\frac{1}{2}}^2}{r_1^2} & & & & & \\ +\frac{r_{1\frac{1}{2}}^2}{r_2^2} & -\frac{r_{1\frac{1}{2}}^2+r_{2\frac{1}{2}}^2}{r_2^2} & +\frac{r_{2\frac{1}{2}}^2}{r_2^2} & & & & \\ & +\frac{r_{2\frac{1}{2}}^2}{r_3^2} & -\frac{r_{2\frac{1}{2}}^2+r_{3\frac{1}{2}}^2}{r_3^2} & +\frac{r_{3\frac{1}{2}}^2}{r_3^2} & & & \\ & & \ddots & \ddots & \ddots & & \\ & & & +\frac{r_{N-2\frac{1}{2}}^2}{r_{N-2}^2} & -\frac{r_{N-2\frac{1}{2}}^2+r_{N-1\frac{1}{2}}^2}{r_{N-2}^2} & +\frac{r_{N-1\frac{1}{2}}^2}{r_{N-2}^2} & \\ & & & & +\frac{r_{N-1\frac{1}{2}}^2}{r_{N-1}^2} & -\frac{r_{N-1\frac{1}{2}}^2+r_{N-\frac{1}{2}}^2}{r_{N-1}^2} & +\frac{r_{N-\frac{1}{2}}^2}{r_{N-1}^2} \\ & & & & & +2\frac{r_{N-\frac{1}{2}}^2}{r_N^2} & -2\frac{r_{N-\frac{1}{2}}^2}{r_N^2} \end{pmatrix}. \tag{B3}$$

Thus, the discretized form of the spherical Bessel differential Eq. (B1) can be written as:

$$R_{\mathrm{A}}^2\left[k_m[k_m+1]\mathrm{diag}\left(\frac{1}{r_1^2}, \ldots, \frac{1}{r_N^2}\right) - \hat{\Delta}_r\right]\boldsymbol{\mathcal{R}}_{nm}(r) = \kappa_{nm}^2\boldsymbol{\mathcal{R}}_{nm}(r), \tag{B4}$$

where each of the N eigenvectors

$$\boldsymbol{\mathcal{R}}_{nm}(r) = (\boldsymbol{\mathcal{R}}_{nm}(r_1), \dots, \boldsymbol{\mathcal{R}}_{nm}(r_N))^{\mathrm{T}} \tag{B5}$$

contains the values of the discretized eigenfunctions $\boldsymbol{\mathcal{R}}_{nm}(r_i)$. It is convenient to normalize the eigenfunctions as:

$$\sum_{i=1}^{N} |\boldsymbol{\mathcal{R}}_{nm}(r_i)|^2 = 1 \tag{B6}$$

or in integral form:

$$\int_{R_A}^{R_P} \mathrm{d}r \boldsymbol{\mathcal{R}}_{nm}(r) \boldsymbol{\mathcal{R}}^*_{nm}(r) = h \tag{B7}$$

with the step size h given in Eq. (B2).

Furthermore, the numerically determined eigenfunctions obeys the scaling on the alveolar surface $R_A = r_1$:

$$\frac{\boldsymbol{\mathcal{R}}_{nm}(r_1)}{R_{nm}(R_A)} = \frac{\boldsymbol{\mathcal{R}}_{nm}(r_i)}{R_{nm}(r_i)}, \tag{B8}$$

where $R_{nm}(R_A) = 1/\kappa^2_{nm}$, see Eq. (97) in [28].

Appendix C. Lineshape in the static dephasing regime

In the static dephasing regime, the lineshape can be obtained as a histogram over the local Larmor frequency $\omega(\mathbf{r})$, given in Eq. (1) [52]:

$$p_{\mathrm{SD}}(\omega) = \frac{1}{V} \int_V \mathrm{d}^3\mathbf{r} \delta(\omega - \omega(\mathbf{r})) \tag{C1}$$

$$= \frac{3\eta}{2[1-\eta]} \int_1^{\eta^{-\frac{1}{3}}} \mathrm{d}\rho \rho^2 \int_0^{\pi} \mathrm{d}\theta \sin(\theta) \delta\left(\omega - \delta\omega \frac{3\cos^2(\theta) - 1}{\rho^2}\right), \tag{C2}$$

where δ denotes Dirac's delta distribution and the substitution $\rho R_A = r$ was applied. Obviously, the lineshape is restricted to the interval $-\delta\omega \leqslant \omega \leqslant +2\delta\omega$. The general property of Dirac's delta distribution for an arbitrary function $q(\theta)$

$$\delta(q(\theta)) = \sum_i \frac{\delta(\theta - \theta_i)}{|q'(\theta_i)|}, \tag{C3}$$

where $q(\theta_i) = 0$, is applied. In this case, the function $q(\theta)$ is the argument of the Dirac-distribution $q(\theta) = \omega - \delta\omega[3\cos^2(\theta) - 1]/\rho^2$ with the single zero $\theta_1 = \arccos\left(\sqrt{[\rho^2\omega/\delta\omega - 1]/3}\right)$. Thus, the polar integral can be carried out to obtain:

$$p_{\mathrm{SD}}(\omega) = \frac{\sqrt{3}}{2} \frac{\eta}{1-\eta} \frac{1}{\delta\omega} \int_1^{\eta^{-\frac{1}{3}}} \frac{\mathrm{d}\rho\rho^4}{\sqrt{1 + \frac{\omega}{\delta\omega}\rho^2}} \Theta\left(1 + \frac{\omega}{\delta\omega}\rho^2\right) \Theta\left(2 - \frac{\omega}{\delta\omega}\rho^2\right), \tag{C4}$$

where the Heaviside step function is denoted as Θ. This integral can be solved and the lineshape is given in Eq. (43). The function f can be rewritten with the identity $\operatorname{arcsinh}(x) = \ln\left(x + \sqrt{x^2+1}\right)$:

$$f\left(\frac{\omega}{\delta\omega}\right) = \begin{cases} \sqrt{-\frac{\delta\omega}{\omega}}\left[\frac{\pi}{2} - \arcsin\left(\sqrt{-\frac{\omega}{\delta\omega}}\right)\right] & \text{for } -1 \leqslant \frac{\omega}{\delta\omega} \leqslant -\eta^{\frac{2}{3}} \\ \left[\frac{1}{\eta}\frac{2}{3}\frac{\omega}{\delta\omega} - \frac{1}{\sqrt[3]{\eta}}\right]\sqrt{1 + \eta^{-\frac{2}{3}}\frac{\omega}{\delta\omega}} & \text{for } -\eta^{\frac{2}{3}} \leqslant \frac{\omega}{\delta\omega} \leqslant 2\eta^{\frac{2}{3}} \\ \quad + \sqrt{\frac{\delta\omega}{\omega}}\left[\operatorname{arcsinh}\left(\frac{1}{\sqrt[3]{\eta}}\sqrt{\frac{\omega}{\delta\omega}}\right) - \operatorname{arcsinh}\left(\sqrt{\frac{\omega}{\delta\omega}}\right)\right] & \\ \sqrt{\frac{\delta\omega}{\omega}}\left[\frac{\sqrt{6}}{3} + \operatorname{arcsinh}\left(\sqrt{2}\right) - \operatorname{arcsinh}\left(\sqrt{\frac{\omega}{\delta\omega}}\right)\right] & \text{for } 2\eta^{\frac{2}{3}} \leqslant \frac{\omega}{\delta\omega} \leqslant 2. \end{cases} \tag{C5}$$

The intermediate intervals $-\eta^{\frac{2}{3}}\delta\omega \leqslant \omega \leqslant 2\eta^{\frac{2}{3}}\delta\omega$ can be divided in two intervals due to the sign changes in the arcsinh-function:

$$f\left(\frac{\omega}{\delta\omega}\right) = \begin{cases} \left[\frac{1}{\eta}\frac{2}{3}\frac{\omega}{\delta\omega} - \frac{1}{\sqrt[3]{\eta}}\right]\sqrt{1 + \eta^{-\frac{2}{3}}\frac{\omega}{\delta\omega}} & \text{for } -\eta^{\frac{2}{3}} \leqslant \frac{\omega}{\delta\omega} \leqslant 0 \\ \quad + \sqrt{-\frac{\delta\omega}{\omega}}\left[\arcsin\left(\frac{1}{\sqrt[3]{\eta}}\sqrt{-\frac{\omega}{\delta\omega}}\right) - \arcsin\left(\sqrt{-\frac{\omega}{\delta\omega}}\right)\right] & \\ \left[\frac{1}{\eta}\frac{2}{3}\frac{\omega}{\delta\omega} - \frac{1}{\sqrt[3]{\eta}}\right]\sqrt{1 + \eta^{-\frac{2}{3}}\frac{\omega}{\delta\omega}} & \text{for } 0 \leqslant \frac{\omega}{\delta\omega} \leqslant 2\eta^{\frac{2}{3}}. \\ \quad + \sqrt{\frac{\delta\omega}{\omega}}\left[\operatorname{arcsinh}\left(\frac{1}{\sqrt[3]{\eta}}\sqrt{\frac{\omega}{\delta\omega}}\right) - \operatorname{arcsinh}\left(\sqrt{\frac{\omega}{\delta\omega}}\right)\right] & \end{cases} \tag{C6}$$

Knowing this function, the lineshape can be obtained from Eq. (43) and is visualized in Fig. 10. The corresponding magnetization $M_{\mathrm{SD}}(t)$ can be obtained as:

$$M_{\mathrm{SD}}(t) = \int_V \mathrm{d}^3\mathbf{r} m_0 \mathrm{e}^{-\mathrm{i}\omega(\mathbf{r})t} \tag{C7}$$

$$= M_0 \frac{3\eta}{1-\eta} \int_0^1 \mathrm{d}x \int_1^{\eta^{-\frac{1}{3}}} \mathrm{d}z z^2 \mathrm{e}^{-\mathrm{i}\delta\omega t \frac{3x^2-1}{z^2}} \tag{C8}$$

$$= M_0 \frac{h\left(\eta^{\frac{2}{3}}\delta\omega t\right) - \eta h(\delta\omega t)}{1-\eta}, \tag{C9}$$

where the h-function is given as:

$$h(y) = \mathrm{e}^{-2\mathrm{i}y} + \mathrm{e}^{\mathrm{i}y}[1+\mathrm{i}]\sqrt{\frac{\pi y}{6}}\operatorname{erf}\left([1+\mathrm{i}]\sqrt{\frac{3y}{2}}\right) + \sqrt{2\pi}[1-\mathrm{i}]y^{\frac{3}{2}} \int_0^1 \mathrm{d}x [3x^2-1]^{\frac{3}{2}} \operatorname{erf}\left([1+\mathrm{i}]\sqrt{y\frac{3x^2-1}{2}}\right). \tag{C10}$$

References

[1] F. Carinci, C. Meyer, F.A. Breuer, P.M. Jakob, In vivo imaging of the spectral line broadening of the human lung in a single breathhold, J. Magn. Reson. Imaging 44 (3) (2016) 745–757.

[2] E.J.R. van Beek, J.M. Wild, H.-U. Kauczor, W. Schreiber, J.P. Mugler, E.E. de Lange, Functional MRI of the lung using hyperpolarized 3-helium gas, J. Magn. Reson. Imaging 20 (2004) 540–554.

[3] D.A. Yablonskiy, A.L. Sukstanskii, J.C. Leawoods, D.S. Gierada, G.L. Bretthorst, S. S. Lefrak, J.D. Cooper, M.S. Conradi, Quantitative in vivo assessment of lung microstructure at the alveolar level with hyperpolarized 3He diffusion mri, Proc. Natl. Acad. Sci. USA 99 (2002) 3111–3116.

[4] J. Parra-Robles, J.M. Wild, The influence of lung airways branching structure and diffusion time on measurements and models of short-range ^{3}He gas MR diffusion, J. Magn. Reson. 225 (2012) 102–113.

[5] D.A. Yablonskiy, A.L. Sukstanskii, J.C. Woods, D.S. Gierada, J.D. Quirk, J.C. Hogg, J.D. Cooper, M.S. Conradi, Quantification of lung microstructure with hyperpolarized ^{3}He diffusion MRI, J. Appl. Physiol. 107 (2009) 1258–1265.

[6] R. Trampel, J.H. Jensen, R.F. Lee, I. Kamenetskiy, G. McGuinness, G. Johnson, Diffusional kurtosis imaging in the lung using hyperpolarized ^{3}He, Magn. Reson. Med. 56 (2006) 733–737.

[7] R. Mulkern, S. Haker, H. Mamata, E. Lee, D. Mitsouras, K. Oshio, M. Balasubramanian, H. Hatabu, Lung parenchymal signal intensity in MRI: a technical review with educational aspirations regarding reversible versus irreversible transverse relaxation effects in common pulse sequences, Concepts Magn. Reson. Part A 43A (2014) 29–53.

[8] J. Zapp, S. Domsch, S. Weingärtner, L.R. Schad, Gaussian signal relaxation around spin echoes: implications for precise reversible transverse relaxation quantification of pulmonary tissue at 1.5 and 3 Tesla, Magn. Reson. Med. 77 (5) (2017) 1938–1945.

[9] L.R. Buschle, F.T. Kurz, T. Kampf, W.L. Wagner, J. Duerr, W. Stiller, P. Konietzke, F. Wünnemann, M.A. Mall, M.O. Wielpütz, H.P. Schlemmer, C.H. Ziener, Dephasing and diffusion on the alveolar surface, Phys. Rev. E 95 (2-1) (2017) 022415.

[10] J.R. Reichenbach, F. Schweser, B. Serres, A. Deistung, Quantitative susceptibility mapping: concepts and applications, Clin. Neuroradiol. 25 (2015) 225–230.

[11] J.P. Marques, R. Bowtell, Application of a Fourier-based method for rapid calculation of field inhomogeneity due to spatial variation of magnetic susceptibility, Concepts Magn. Reson. Part B Magn. Reson. Eng. 25 (2005) 65–78.

[12] Y.C. Cheng, E.M. Haacke, Y.J. Yu, An exact form for the magnetic field density of states for a dipole, Magn. Reson. Imaging 19 (2001) 1017–1023.

[13] F.T. Kurz, T. Kampf, S. Heiland, M. Bendszus, H.-P. Schlemmer, C.H. Ziener, Theoretical model of the single spin-echo relaxation time for spherical magnetic perturbers, Magn. Reson. Med. 71 (2014) 1888–1895.

[14] F.T. Kurz, T. Kampf, L.R. Buschle, H.-P. Schlemmer, S. Heiland, M. Bendszus, C.H. Ziener, Microstructural analysis of peripheral lung tissue through CPMG inter-echo time R2 dispersion, PloS One 10 (2015) e0141894.
[15] R.A. Christman, D.C. Ailion, T.A. Case, C.H. Durney, A.G. Cutillo, S. Shioya, K.C. Goodrich, A.H. Morris, Comparison of calculated and experimental NMR spectral broadening for lung tissue, Magn. Reson. Med. 35 (1996) 6–13.
[16] D. Le Bihan, E. Breton, D. Lallemand, P. Grenier, E. Cabanis, M. Laval-Jeantet, MR imaging of intravoxel incoherent motions: application to diffusion and perfusion in neurologic disorders, Radiology 161 (2) (1986) 401–407.
[17] H.C. Torrey, Bloch equations with diffusion terms, Phys. Rev. 104 (1956) 563–565.
[18] J.H. Jensen, R. Chandra, NMR relaxation in tissues with weak magnetic inhomogeneities, Magn. Reson. Med. 44 (2000) 144–156.
[19] A.L. Sukstanskii, D.A. Yablonskiy, Gaussian approximation in the theory of MR signal formation in the presence of structure-specific magnetic field inhomogeneities. Effects of impermeable susceptibility inclusions, J. Magn. Reson. 167 (2004) 56–67.
[20] L.R. Buschle, F.T. Kurz, T. Kampf, S.M.F. Triphan, H.-P. Schlemmer, C.H. Ziener, Diffusion-mediated dephasing in the dipole field around a single spherical magnetic object, Magn. Reson. Imaging 33 (2015) 1126–1145.
[21] D. Le Bihan, E. Breton, D. Lallemand, M.L. Aubin, J. Vignaud, M. Laval-Jeantet, Separation of diffusion and perfusion in intravoxel incoherent motion MR imaging, Radiology 168 (2) (1988) 497–505.
[22] F. Carinci, C. Meyer, F.A. Breuer, S. Triphan, M. Choli, P.M. Jakob, Blood volume fraction imaging of the human lung using intravoxel incoherent motion, J. Magn. Reson. Imaging 41 (2015) 1454–1464.
[23] E.O. Stejskal, J.E. Tanner, Spin diffusion measurements: spin echoes in the presence of a time-dependent field gradient, J. Chem. Phys. 42 (1) (1965) 288–292.
[24] M. Horimoto, T. Koyama, H. Mishina, T. Asakura, M. Murao, Blood flow velocity in pulmonary microvessels of bullfrog, Respir. Physiol. 37 (1) (1979) 45–59.
[25] C.H. Ziener, T. Kampf, G. Reents, H.P. Schlemmer, W.R. Bauer, Spin dephasing in a magnetic dipole field, Phys. Rev. E 85 (2012) 051908.
[26] C.H. Ziener, F.T. Kurz, T. Kampf, Free induction decay caused by a dipole field, Phys. Rev. E 91 (2015) 032707.
[27] J.A. Stratton, P.M. Morse, L.J. Chu, J.D.C. Little, F.J. Corbató, Spheroidal Wave Functions, Chapman and Hall, London, 1956.
[28] C.H. Ziener, F.T. Kurz, L.R. Buschle, T. Kampf, Orthogonality, Lommel integrals and cross product zeros of linear combinations of Bessel functions, SpringerPlus 4 (2015) 390.
[29] C. Flammer, Spheroidal Wave Functions, Stanford University Press, Stanford, 1957.
[30] J. Meixner, F.W. Schäfke, G. Wolf, Mathieu Functions and Spheroidal Functions and their Mathematical Foundations, Springer-Verlag, Berlin Heidelberg, 1980.
[31] L.-W. Li, X.-K. Kang, M.-S. Leong, Spheroidal Wave Functions in Electromagnetic Theory, John Wiley and Sons, New York, 2002.
[32] A. Osipov, V. Rokhlin, H. Xiao, Prolate Spheroidal Wave Functions of Order Zero, Springer Science+Business Media, New York, 2013.
[33] D.S. Grebenkov, Analytical solution for restricted diffusion in circular and spherical layers under inhomogeneous magnetic fields, J. Chem. Phys. 128 (2008) 134702.
[34] A.G. Cutillo, Application of Magnetic Resonance to the Study of Lung, Futura Publishing Company, Inc., Armonk, NY, 1996.
[35] A. Abragam, Principles of Nuclear Magnetism, Oxford University Press, 1961.
[36] R.R. Ernst, Numerical Hilbert transform and automatic phase correction in magnetic resonance spectroscopy, J. Magn. Reson. 1 (1) (1969) 7–26.
[37] F.T. Kurz, C.H. Ziener, M. Rückl, A. Hahn, V.J.F. Sturm, K. Zhang, L.R. Buschle, M. Bendszus, S. Heiland, H.P. Schlemmer, W.R. Bauer, T. Kampf, The influence of spatial patterns of capillary networks on transverse relaxation, Magn. Reson. Imaging 40 (2017) 31–47.
[38] C.H. Ziener, T. Kampf, G. Melkus, P.M. Jakob, W.R. Bauer, Scaling laws for transverse relaxation times, J. Magn. Reson. 184 (2007) 169–175.
[39] P.A. Bottomley, Selective volume method for performing localized NMR spectroscopy, US Patent 4,480,228, 1984.
[40] P.A. Bottomley, Spatial localization in NMR spectroscopy in vivo, Ann. NY Acad. Sci. 508 (1987) 333–348.
[41] J.F. Schenck, The role of magnetic susceptibility in magnetic resonance imaging: MRI magnetic compatibility of the first and second kinds, Med. Phys. 23 (6) (1996) 815–850.
[42] K.C. Stone, R.R. Mercer, B.A. Freeman, L.Y. Chang, J.D. Crapo, Distribution of lung cell numbers and volumes between alveolar and nonalveolar tissue, Am. Rev. Respir. Dis. 146 (1992) 454–456.
[43] M. Ochs, J.R. Nyengaard, A. Jung, L. Knudsen, M. Voigt, T. Wahlers, J. Richter, H. J. Gundersen, The number of alveoli in the human lung, Am. J. Respir. Crit. Care Med. 169 (2004) 120–124.
[44] E.M. Scarpelli, The alveolar surface network: a new anatomy and its physiological significance, Anat. Rec. 251 (1998) 491–527.
[45] E. Namati, J. Thiesse, J. de Ryk, G. McLennan, Alveolar dynamics during respiration: are the pores of Kohn a pathway to recruitment?, Am J. Respir. Cell Mol. Biol. 38 (2008) 572–578.
[46] W.R. Bauer, W. Nadler, M. Bock, L.R. Schad, C. Wacker, A. Hartlep, G. Ertl, The relationship between the BOLD-induced T2 and T2*: a theoretical approach for the vasculature of myocardium, Magn. Reson. Med. 42 (1999) 1004–1010.
[47] C.H. Ziener, T. Kampf, G. Melkus, P.M. Jakob, H.P. Schlemmer, W.R. Bauer, Signal evolution in the local magnetic field of a capillary – analogy to the damped driven harmonic oscillator, Magn. Reson. Imaging 30 (2012) 540–553.
[48] M. Herberthson, E. Özarslan, H. Knutsson, C.F. Westin, Dynamics of local magnetization in the eigenbasis of the Bloch-Torrey operator, J. Chem. Phys. 146 (12) (2017) 124201.
[49] L.R. Buschle, C.H. Ziener, K. Zhang, V.J.F. Sturm, T. Kampf, A. Hahn, G. Solecki, F. Winkler, M. Bendszus, S. Heiland, H.P. Schlemmer, F.T. Kurz, Vessel radius mapping in an extended model of transverse relaxation, Magn. Reson. Mater. Phy. 31 (2018) 531–551.
[50] C.H. Ziener, H.P. Schlemmer, The inverse Laplace transform of the modified Lommel functions, Integ. Transf. Spec. F 24 (2013) 141–155.
[51] C.H. Ziener, S. Glutsch, P.M. Jakob, W.R. Bauer, Spin dephasing in the dipole field around capillaries and cells: numerical solution, Phys. Rev. E 80 (2009) 046701.
[52] C.H. Ziener, W.R. Bauer, P.M. Jakob, Frequency distribution and signal formation around a vessel, Magn. Reson. Mater. Phy. 18 (2005) 225–230.